Hole Effective Masses as a Booster of Self-Consistent Six-Band $k \cdot p$ Simulation in Inversion Layers of pMOSFETs

Ming-Jer Chen, *Senior Member, IEEE*, Chien-Chih Lee, *Student Member, IEEE*, and Kuan-Hao Cheng

***Abstract*—Self-consistently solving the Schrödinger and Poisson's equations in the six-band $k \cdot p$ context can yield the valence-band structure in the inversion layers of pMOSFETs. In this numerically demanding process, the central processing unit (CPU) time is extraordinarily long. To overcome the hurdle, we construct a novel computational accelerator to intrinsically boost a self-consistent six-band $k \cdot p$ simulation. This accelerator comprises a triangular-potential-based six-band $k \cdot p$ simulator, a hole effective mass approximation (EMA) technique, and an electron analogy version of the self-consistent Schrödinger and Poisson's equations solver. The outcome of the accelerator furnishes the initial solution of the confining electrostatic potential and is likely close to the realistic one, which is valid for different temperatures, substrate doping concentrations, inversion hole densities, and surface orientations. The results on (001) and (110) substrates are supported by those published in the literature. The overall CPU time is reduced down to around 8% of that without the accelerator. This is the first successful demonstration of the EMA in the self-consistent hole subband structure calculation. The application of the proposed accelerator to more general situations is projected as well.**

***Index Terms*—Effective mass, hole, model, metal–oxide–semiconductor field-effect transistors (MOSFETs), Schrödinger and Poisson's equations, simulation, two-dimensional hole gas (2DHG), valence-band structure.**

I. Introduction

As WIDELY recognized, the merits of the effective mass approximation (EMA) in the conduction-band valleys [1] are twofold: First, the computation task to execute self-consistent Schrödinger and Poisson's equations solving in the inversion layers of nMOSFETs is straightforward [1]. Second, the combination of the resulting subband energy levels and the corresponding electron effective masses can constitute the conduction-band structure in the inversion layers of nMOSFETs [1].

On the other hand, the valence-band structure in the inversion layers of pMOSFETs is quite complicated in terms of the strong anisotropy and nonparabolicity of the hole subbands, as readily described by a six-band $k \cdot p$ method [2]. To simplify the hole subband structure calculation, a triangular-potential approximation can be employed [3]. While incorporating the six-band $k \cdot p$ method into the Schrödinger and Poisson's equations to solve the more practical problems, the undertaken numerical calculation becomes so demanding that the overall central processing unit (CPU) time is extremely huge, which might prohibit the valence-band structure calculation in a tolerable time. Thus, reducing the CPU time as greatly as possible in the self-consistent six-band $k \cdot p$ framework is absolutely a relevant issue.

Recently, De Michielis *et al.* [4] exhibited one such effort in terms of an analytical model for the in-plane energy dispersion, followed by a sophisticated interpolation method by Pham *et al.* [5]. However, to produce the hole subband structure as accurately as possible, a very fine discretization in the 2-D k-space is essential, without accounting for the analytical model [4] or the interpolation method [5]. It is also noticed that Low *et al.* [6] explored the effectiveness of one-band EMA in capturing the electrostatics property of six hole bands. In addition, the energy dependence of the hole effective mass was also taken into account in the development of the analytical model by De Michielis *et al.* [4]. Until now, however, the superior ability of the hole EMA to speed up the self-consistent six-band confined $k \cdot p$ calculation was not yet demonstrated as a function of the temperature, the substrate doping concentration, the inversion hole density, and the surface orientation.

In this paper, we construct a new computational accelerator to intrinsically boost a self-consistent six-band $k \cdot p$ simulator. A very fine grid in the 2-D k-space is adopted, without the use of the efficient discretization approach [4], [5]. The core of the accelerator lies in the hole EMA whose formulation, which is essentially different from those of [4] and [6], can accommodate the use of an electron analogy version of the self-consistent Schrödinger and Poisson's equations solver. In the following sections, we will systematically demonstrate the establishment of the accelerator and its ability to overcome the computational burden in the confined $k \cdot p$ simulation.

II. Computational Acceleration

The simulation methodology constructed in this paper, as shown in Fig. 1 in terms of a flowchart, consists of the two main blocks: 1) the new computational acceleration and 2) the self-consistent simulation framework. The connection between

Manuscript received September 29, 2010; revised November 19, 2010 and December 17, 2010; accepted December 20, 2010. Date of publication February 10, 2011; date of current version March 23, 2011. This work was supported by the National Science Council of Taiwan under Contract NSC 97-2221-E-009-155-MY3. The review of this paper was arranged by Editor A. Schenk.

M.-J. Chen and C.-C. Lee are with the Department of Electronics Engineering and Institute of Electronics, National Chiao Tung University, Hsinchu 300, Taiwan (e-mail: chenmj@faculty.nctu.edu.tw).

K.-H. Cheng is with the Ministry of National Defense, Taipei 10048, Taiwan.

Color versions of one or more of the figures in this paper are available online at http://ieeexplore.ieee.org.

Digital Object Identifier 10.1109/TED.2011.2105271

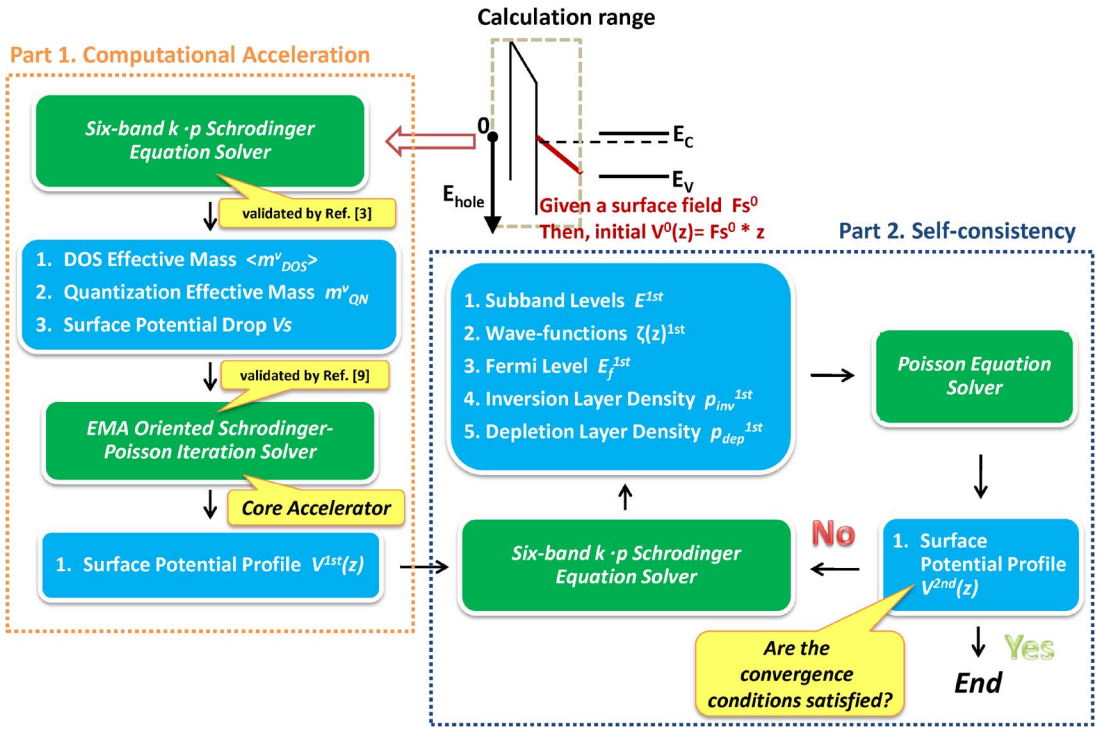

Fig. 1. Flowchart of the simulation methodology in the inversion layer of pMOSFET. The methodology consists of two parts: 1) the computational acceleration part in order to enhance the convergence speed and 2) the self-consistent part in order to certify the tolerable error. The green blocks refer to the simulation methodology, and the turquoise blocks refer to the outputs from the upper level simulator.

the two is the confining potential profile, which is the outcome of the computational accelerator and serves as the input to the subsequent self-consistent simulator. Throughout the paper, the energy reference point exactly falls on the classical valence-band edge at the SiO_2/Si interface, as illustrated in Fig. 1.

A. Triangular-Potential-Based Six-Band $k \cdot p$ Simulator

In the six-band $k \cdot p$ context, the in-plane wave equation along the quantum confinement direction z can read as

$$\left[-H_{LK}\left(k_x, k_y, k_z = -i\frac{d}{dz}\right) + qV(z)\right] \cdot \xi_{k_x,k_y}(z) = E(k_x, k_y) \cdot \xi_{k_x,k_y}(z) \quad (1)$$

where $V(z)$ is the confining electrostatic potential, $\xi_{k_x,k_y}(z)$ is the wave function, and E is the energy of holes. The origin $z = 0$ represents the SiO_2/Si interface. H_{LK} in (1) is the Luttinger–Kohn Hamiltonian [7] with the split-off energy Δ of 44 meV in the absence of the quantum confinement and with the Luttinger parameters of $\gamma_1 = 4.22$, $\gamma_2 = 0.39$, and $\gamma_3 = 1.44$ [8]. The computational accelerator starts with the initial triangular-potential profile: $V^0(z) = F_s^o z$, where F_s^o is the initial surface field. The simulation range of interest in the z-direction is divided into a mesh of N_z points in the interval $[0, Z_{\max}]$, where $Z_{\max}$ is equal to $6E_{\max}/\mathrm{q}F_s^o$ for $E_{\max} = 0.3$ eV [3]. Then, (1) becomes a $6N_z \times 6N_z$ eigenvalue problem. The grid number on $k_x - k_y$ space is 101×101 in a Cartesian coordinate system. In addition, a polar coordinate system is employed where the grid number on $k - \theta$ space is 101×101. The boundary conditions are $\xi_{k_x,k_y}(0) = 0$ and $\xi_{k_x,k_y}(Z_{\max}) = 0$. The solution of the eigenvalue problem yields $E(k_x, k_y)$ and normalized $\xi_{k_x,k_y}(z)$. The Fermi level can then be determined. To deal with the (110) case, a rotation transformation from the original (001) k space to the (110) k' space is required: $k_x' = -k_z$, $k_y' = (1/\sqrt{2})(k_x - k_y)$, and $k_z' = (1/\sqrt{2})(k_x + k_y)$. The resulting hole subband energy contours, subband level, and Fermi level on the (001) and (110) surface orientations were found to be in good agreement with those of Fischetti *et al.* [3] (not shown here).

B. Hole-EMA Technique

As shown in Fig. 1, the outcomes of the triangular-potential-based six-band $k \cdot p$ simulator contain the constant-energy contours in the k plane, the subband energy levels, the surface potential, and the Fermi level E_f of the system. At this point, we demonstrate how to apply the EMA technique to create the two important parameters in this paper: 1) hole quantization effective mass and 2) hole density-of-states (DOS) effective mass. First, the DOS function of subband ν can be determined in the Cartesian coordinate system [2] by

$$\mathrm{DOS}_\nu(E) = U(E - E_\nu)\frac{1}{(2\pi)^2} \times \frac{Area_\nu^{\mathrm{k-space}}(E + dE) - Area_\nu^{\mathrm{k-space}}(E)}{dE} \quad (2)$$

and in the polar coordinate system [3] by

$$\mathrm{DOS}_\nu(E) = U(E - E_\nu)\frac{1}{(2\pi)^2}\int_0^{2\pi} \frac{K_\nu(E,\theta)}{\left|\frac{dE}{dK}\right|_{K_\nu(E,\theta)}} d\theta. \quad (3)$$

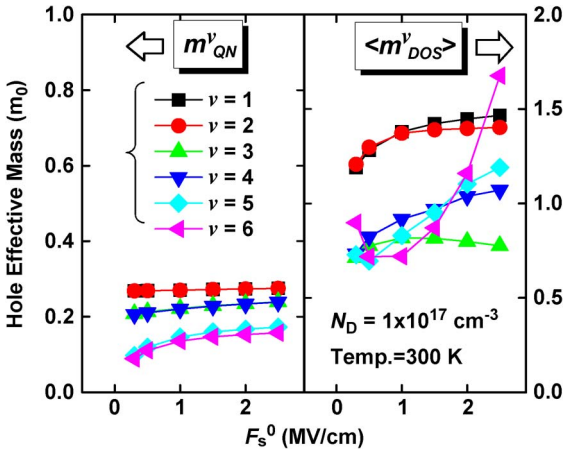

Fig. 2. Calculated hole quantization effective masses and DOS effective masses versus the initial surface field in the simulation flowchart in Fig. 1.

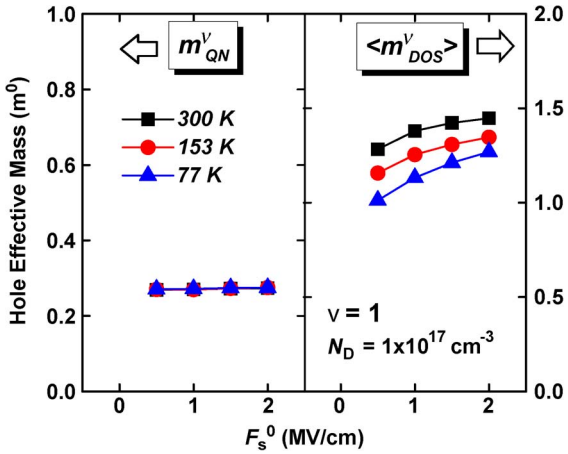

Fig. 3. Calculated hole quantization effective masses and DOS effective masses versus the initial surface field for different temperatures of 77, 153, and 300 K in the simulation flowchart in Fig. 1.

Here, $Area_\nu^{\text{k-space}}(E+dE) - Area_\nu^{\text{k-space}}(E)$ represents the area between the E and $E+dE$ lines of subband ν in the k plane, E_ν is the energy level of subband ν, $U(E)$ represents the unit step function of energy, and magnitude K_ν is a function of both energy E and angle θ. The DOS effective mass of subband ν can be obtained accordingly: $m^\nu_{\text{DOS}}(E) = 2\pi\hbar^2 \times \text{DOS}_\nu(E)$. While averaging the DOS effective mass of subband ν over the energy, the dependence on hole density distribution must be taken into account as follows:

$$\langle m^\nu_{\text{DOS}} \rangle = \frac{\int m^\nu_{\text{DOS}}(E) f(E) \cdot \text{DOS}_\nu(E) dE}{\int f(E) \cdot \text{DOS}_\nu(E) dE} \tag{4}$$

where $f(E)$ is the Fermi–Dirac distribution function including the Fermi level E_f. Note that the formalism (4) is completely different from those of [4] and [6]. As to quantization effective mass of subband ν, it can be readily assessed in a triangular-potential sense [1], i.e.,

$$m^\nu_{\text{QN}} = \frac{\hbar^2}{2}(E_\nu)^{-3}\left(\frac{3}{2}\pi q F_S^0\left(j+\frac{3}{4}\right)\right)^2 \tag{5}$$

where j reflects the status of the wave function at subband minimum (e.g., $j=0$ for the ground state and 1 for the first excited state). Note that, under the quantum confinement conditions, E_5 and E_6 in (5) no longer refer to the pure (bulk) split-off holes (SH) due to the mixing with a fraction of light holes. In other words, E_5 and E_6 should be seen as individual subbands with respect to the classical reference point, rather than to the bulk split-off energy point (situated 44 meV away), when calculating the quantization effective mass. Both the Cartesian and polar coordinate systems led to nearly the same results. Thus, throughout the paper, the Cartesian coordinate system is adopted, unless mentioned otherwise. The resulting $\langle m^\nu_{\text{DOS}} \rangle$ and m^ν_{QN} versus initial surface field are depicted in Fig. 2 for subband $\nu = 1$ to 6 and Fig. 3 for $\nu = 1$ with different temperatures.

C. Core Accelerator

Analogous to the electron counterparts [9], [10], the simple EMA-oriented Schrödinger–Poisson iterative solving can readily be employed using the aforementioned hole effective masses. First, the Schrödinger equation in pMOSFETs can be written accordingly, i.e.,

$$\left[-\frac{\hbar^2}{2m^\nu_{\text{QN}}}\frac{d^2}{dz^2} + qV(z)\right]\phi(z) = E\phi(z). \tag{6}$$

The energy level $E_{\nu,j}$ of sub-subband j within subband ν and the corresponding normalized wave function $\phi_{\nu,j}(z)$ can be obtained by solving the eigen problem in (6). In addition, using an analogy, the expression of the hole density in the 2DHG case becomes

$$p(z) = \sum_{\nu,j}\frac{\langle m^\nu_{\text{DOS}}\rangle}{2\pi\hbar^2}k_B T \ln\left(1+e^{\frac{E_f - E_{\nu,j}}{kT}}\right)\cdot|\phi_{\nu,j}(z)|^2. \tag{7}$$

The EMA-oriented Schrödinger–Poisson iterative solving in pMOSFETs can therefore be expected to be as fast as nMOSFETs. The Fermi level is determined in the self-consistent loop, given the surface band bending and substrate-doping concentration. The calculation results have been corroborated using the available simulator Schred [9] (not shown here).

As previously mentioned, the calculated hole quantization and DOS effective masses contain information about the anisotropy and nonparabolicity of the subbands. The outcome of the EMA-oriented Schrödinger–Poisson iterative solving, which is the initial solution of the confined potential profile as illustrated in Fig. 1, is likely close to the realistic one. Consequently, a fast convergence in the subsequent self-consistent six-band $k \cdot p$ simulation can be ensured. This is the fact, as will be proved later.

III. Results and Discussion

To confirm the validity of the whole simulation methodology in Fig. 1, we quote the existing self-consistent six-band $k \cdot p$ simulation results [4], [6]. First, in our paper, the following convergence criteria were set for the self-consistent six-band $k \cdot p$ simulator: 1) below 1% error for the surface field and

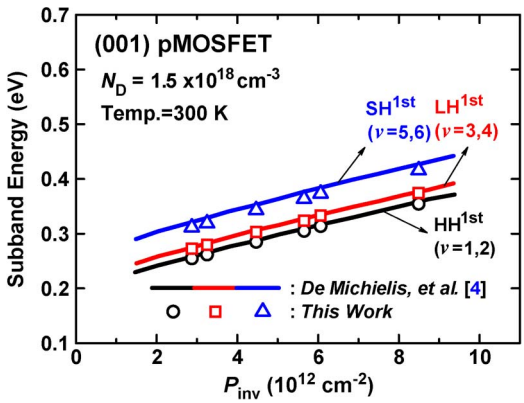

Fig. 4. Calculated (symbols) hole subband energy levels versus inversion carrier density on the (001) surface. The solid lines come from [4] for comparison.

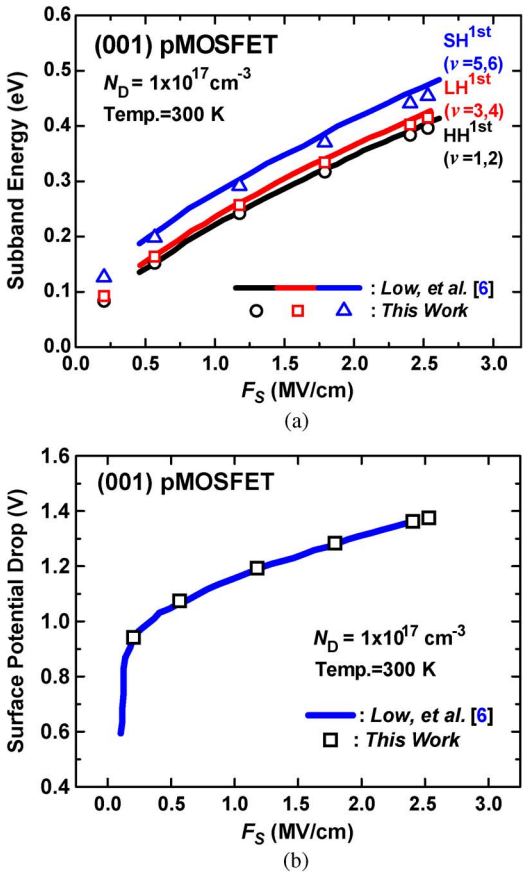

Fig. 5. (a) Calculated (symbols) hole subband energy levels versus surface field on the (001) substrate. The solid lines come from [6] for comparison. (b) Corresponding surface potential versus surface field.

2) 10^{-4} V maximum error for the confining electrostatic potential profile. In addition, the grid number N_z was set at 301.

Fig. 4 depicts the comparison of the simulated subband energy level on (001) substrate versus inversion-layer hole density with that of De Michielis *et al.* [4]. Good agreement is achieved. This is also the case in comparison with those of Low *et al.* [6], as given in Fig. 5 for the subband level and surface potential versus the surface field F_s. A small deviation of SH subbands in Figs. 4 and 5(a) is due to the fact that the subband level in this paper represents the energy minimum

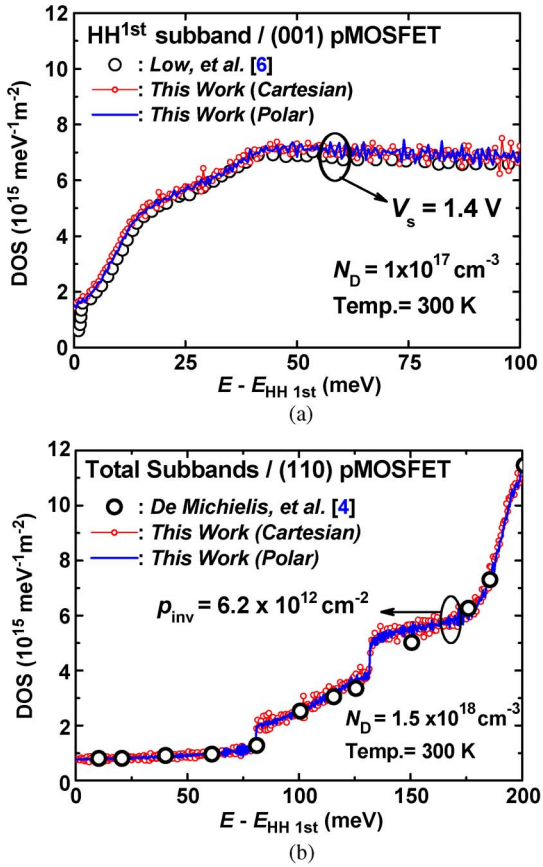

Fig. 6. (a) Simulated DOS function for the first subband on the (001) substrate in our paper. The red and green solid lines are produced from the Cartesian and polar coordinate systems, respectively. The dotted line comes from [6] for comparison. (b) Simulated DOS function for the total subbands on the (110) substrate. The red and green solid lines are produced from the Cartesian and polar coordinate systems, respectively. The dotted line comes from [4].

rather than the gamma point. Further evidence exists in terms of the simulated DOS results, as shown in Fig. 6 for (001) and (110) substrates. Evidently, excellent agreements with those from different sources [4], [6] are obtained. Particularly, a careful observation leads to the argument that, under the same grid number, the simulated DOS in a polar coordinate system is less "noisy" than the Cartesian one, as expected from the numerical analysis point of view.

More importantly, we found that, relative to the conventional self-consistent six-band $k \cdot p$ simulation without the accelerator, the whole computational time with the accelerator included can be substantially reduced. First, the simulation methodology in Fig. 1 can reduce to the conventional self-consistent six-band $k \cdot p$ simulator only, which is achieved by simply removing the accelerator part. The CPU time consumed with and without the accelerator is plotted in Fig. 7 for (001) and (110) substrates. Interestingly, with the accelerator added, the overall CPU time is reduced down to around 8% of that without the accelerator for (001) substrate and 17% for (110) substrate. Note that the relatively large computational time in this paper, as compared with that of [5], is due to a larger mesh number in both k space (101×101) and z-direction ($N_z = 301$), as well as the lower hardware level and operating system. Furthermore, we found that, in all (001) cases under study, no iteration can be needed in

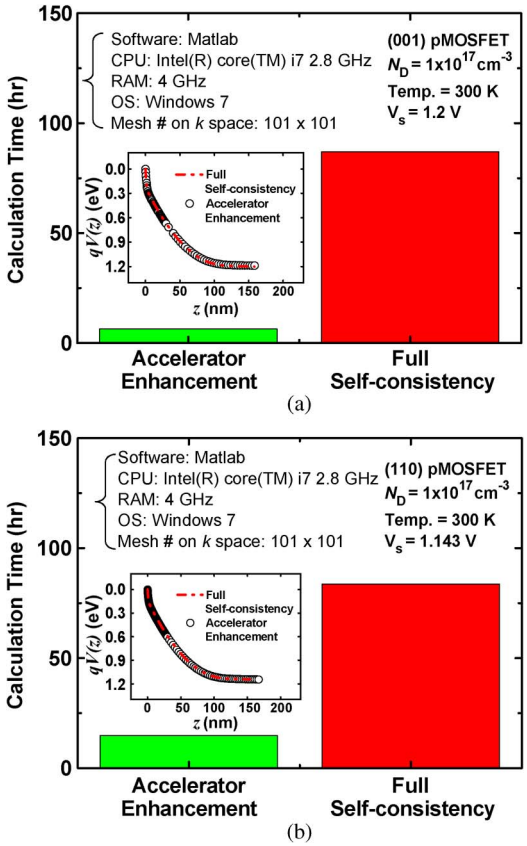

Fig. 7. Comparison of the CPU time between the accelerator-enhanced methodology and the fully self-consistent methodology without the accelerator on the (a) (001) and (b) (110) substrates. The inserted figure shows the corresponding electrostatic potential profiles.

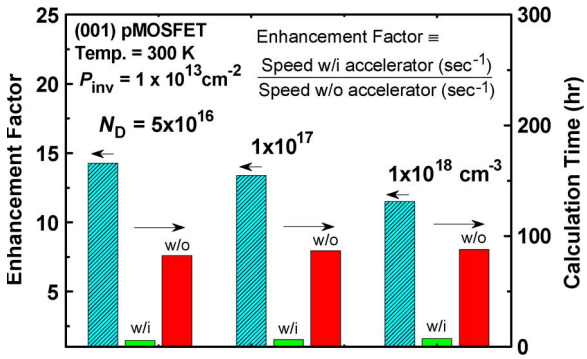

Fig. 8. Computational enhancement factor on the (001) substrate versus the substrate doping concentration under the same inversion hole density of 1×10^{13} cm^{-2}. In addition, the corresponding CPU time with and without the accelerator is shown.

the self-consistent six-band $k \cdot p$ simulator of the methodology. This means that the confining electrostatic potential created by the accelerator is in close proximity of the realistic one, as shown in the inset of Fig. 7(a). Even for the (110) case in Fig. 7(b), only one iteration step is needed to make the specific error satisfied. This explains a slight increase in the CPU time, compared with the (001) case.

In addition, we present in Fig. 8 the enhancement factor of the computational speed as a function of the doping concentration in the substrate while keeping the same inversion carrier

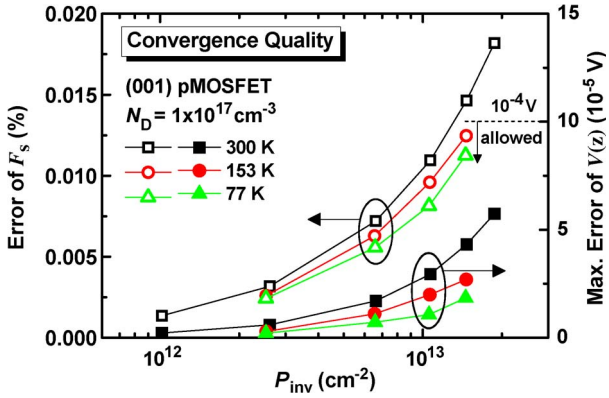

Fig. 9. Convergence quality on the (001) substrate versus the surface field at 77, 153, and 300 K. The convergence conditions in this paper are below 1% error for the surface field and 10^{-4} V maximum error for the confining electrostatic potential profile.

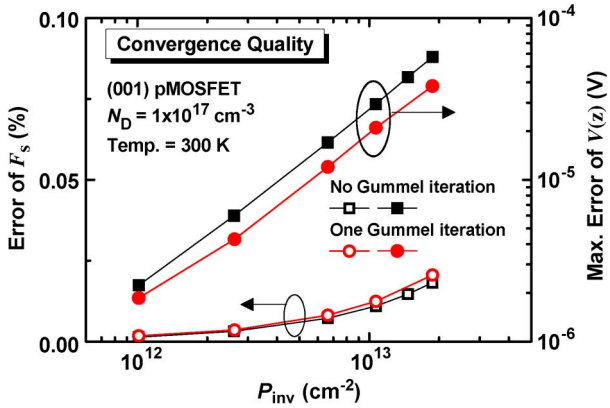

Fig. 10. Comparison of the convergence quality having no Gummel iteration and that with the additional Gummel iteration, which is plotted as a function of the inversion hole density on the (001) substrate at 300 K.

density. In addition, the corresponding CPU time with and without the accelerator is shown. Obviously, the speed enhancement slightly decreases with increasing doping concentration. The increased calculation time as found in the fully self-consistent algorithm itself with increasing doping concentration is primarily due to the nature of solving six-band $k \cdot p$ Schrödinger equation (with the same iteration steps). On the contrary, the increased calculation time in the accelerator-enhanced algorithm is mainly consumed in the triangular-potential-based six-band $k \cdot p$ Schrödinger solver. The larger increasing rate of calculation time in the accelerator-enhanced algorithm leads to the observed trend of the speed enhancement. We also examine the convergence quality in this paper in terms of the errors encountered in the self-consistent simulation part (without any iteration), as shown in Fig. 9 for the (001) substrate plotted versus the inversion hole density with the temperature as a parameter. It is clear that not only the surface field errors but also the potential errors are all far below the corresponding critical errors of 1% and 10^{-4} V, respectively, which is valid for the temperature and inversion-layer hole density range demonstrated. This thereby serves as the corroborating evidence that no Gummel-type iteration can be needed in the (001) self-consistent six-band $k \cdot p$ simulation. However, further analysis

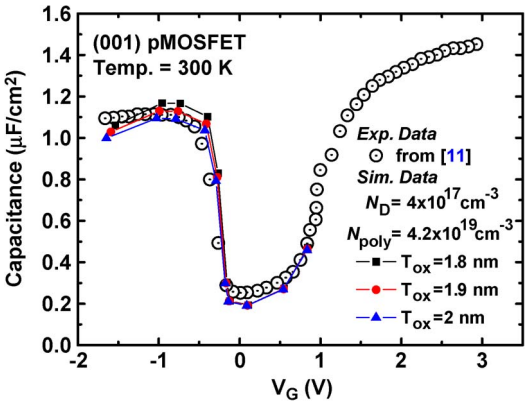

Fig. 11. Comparison of the experimental gate capacitance versus gate voltage curves [11] and those (only in weak- and strong-inversion regions) simulated with the convergence criterion of 10^{-4} V for the confining potential. From the HRTEM image [11], the nominal physical gate oxide thickness is 1.89 nm. However, in the simulation, three different physical gate oxide thicknesses were used to testify the validity of the chosen convergence criterion in this paper.

as depicted in Fig. 10 reveals that, if the more strict convergence criterion is set, additional Gummel iterations may be requested to further reduce the errors. In other words, the lower the order of tolerable error, the more iteration steps needed. Thus, there is a tradeoff between the convergence criterion and the efficiency of the proposed accelerator. However, we want to emphasize that the convergence error of 10^{-4} V as adopted in this paper is adequate. This point can be highlighted in Fig. 11 in terms of the fitting of the experimental gate capacitance versus gate voltage curve [11]. Evidently, the fitting quality with the convergence criterion of 10^{-4} V is acceptable, especially in the weak inversion region, where the gate capacitance changes sharply with the gate voltage.

IV. Projection

At this point, two key points can be drawn. First, the initial solution of the confining potential profile as close to the realistic one as possible is the key to eliminating or reducing the conventionally required Gummel-type iteration steps in the self-consistent six-band $k \cdot p$ simulation. Thus, the CPU time can be substantially lowered. Second, the ability to create such potential profile in advance is the main merit of the proposed hole-EMA-based accelerator. Moreover, we want to stress that the hole-EMA-based accelerator introduced in this paper is simple and feasible. Thus, we can make a projection of the accelerator concerning its general applications.

First, the proposed accelerator can accommodate the strained p-MOSFET case, which is achieved by incorporating the strain Hamiltonian H_{strain} [3], [12] in the $k \cdot p$ context. Second, to adequately deal with the ultrathin-film device, a higher order $k \cdot p$ framework, such as the eight-band $k \cdot p$ one (see [13] for the comparison with the six-band one), may be needed to replace the six-band one in the methodology in Fig. 1. In this case, the space-induced confinement formula may be required rather than the field-induced confinement formula (i.e., triangular-potential well) in this paper. Note that the wave function penetration into the oxide was not taken into account here. However, this issue is considerably important, especially for the ultrathin-film case. The effect of the wave function penetration on the applicability of the proposed accelerator, as well as the possible modification of the accelerator, needs to be further investigated. Finally, the additional issues of other surface orientations or channel materials, which were not addressed in this paper, should, in principle, be able to benefit from the proposed accelerator.

V. Conclusion

We have constructed a new computational accelerator based on a hole EMA, with the aim to intrinsically boost a self-consistent six-band $k \cdot p$ simulation. First, a triangular-potential-based six-band $k \cdot p$ simulation has been performed to produce hole quantization and DOS effective masses. Then, with those hole effective masses as input, an *EMA-oriented Schrödinger–Poisson iterative solving in pMOSFETs* has been executed as rapidly as the electron counterparts. The resulting confining electrostatic potential profile has been proven to match the realistic one, thus ensuring a fast convergence in the subsequent self-consistent six-band $k \cdot p$ simulation. This remains valid for different temperatures, different substrate doping concentrations, different inversion hole densities, and different surface orientations. We have found that the overall CPU time is substantially reduced down to around 8% to 17% of that without the use of the proposed accelerator. The validity of the chosen convergence criteria has been verified. The simulated results have been validated by the published ones obtained from the conventional self-consistent six-band $k \cdot p$ method alone. The application of the proposed accelerator to more general applications has been projected.

References

[1] F. Stern, "Self-consistent results for n-type Si inversion layers," *Phys. Rev. B, Condens. Matter*, vol. 5, no. 12, pp. 4891–4899, Jun. 1972.
[2] R. Oberhuber, G. Zandler, and P. Vogl, "Subband structure and mobility of two-dimensional holes in strained Si/SiGe MOSFETs," *Phys. Rev. B, Condens. Matter*, vol. 58, no. 15, pp. 9941–9948, Oct. 1998.
[3] M. V. Fischetti, Z. Ren, P. M. Solomon, M. Yang, and K. Rim, "Six-band $k \cdot p$ calculation of the hole mobility in silicon inversion layers: Dependence on surface orientation, strain, and silicon thickness," *J. Appl. Phys.*, vol. 94, no. 2, pp. 1079–1095, Jul. 2003.
[4] M. De Michielis, D. Esseni, Y. L. Tsang, P. Palestri, L. Selmi, A. G. O'Neill, and S. Chattopadhyay, "A semianalytical description of the hole band structure in inversion layers for the physically based modeling of pMOS transistors," *IEEE Trans. Electron Devices*, vol. 54, no. 9, pp. 2164–2173, Sep. 2007.
[5] A. T. Pham, B. Meinerzhagen, and C. Jungemann, "A fast $k \cdot p$ solver for hole inversion layers with an efficient 2D k-space discretization," *J. Comput. Electron.*, vol. 7, no. 3, pp. 99–102, Dec. 2008.
[6] T. Low, Y. T. Hou, and M. F. Li, "Improved one-band self-consistent effective mass methods for hole quantization in p-MOSFET," *IEEE Trans. Electron Devices*, vol. 50, no. 5, pp. 1284–1289, May 2003.
[7] J. M. Luttinger and W. Kohn, "Motion of electrons and holes in perturbed periodic fields," *Phys. Rev.*, vol. 97, no. 4, pp. 869–883, Feb. 1955.
[8] P. Lawaetz, "Valence-band parameters in cubic semiconductors," *Phys. Rev. B, Condens. Matter*, vol. 4, no. 10, pp. 3460–3467, Nov. 1971.
[9] Schred. [Online]. Available: http://nanohub.org/resources/schred
[10] D. Vasileska, D. K. Schroder, and D. K. Ferry, "Scaled silicon MOSFETs: Degradation of the total gate capacitance," *IEEE Trans. Electron Devices*, vol. 44, no. 4, pp. 584–587, Apr. 1997.
[11] K. N. Yang, H. T. Huang, M. C. Chang, C. M. Chu, Y. S. Chen, M. J. Chen, Y. M. Lin, M. C. Yu, S. M. Jang, D. C. H. Yu, and M. S. Liang, "A physical model for hole direct tunneling current in P^+ poly-gate PMOSFETs with ultrathin gate oxides," *IEEE Trans. Electron Devices*, vol. 47, no. 11, pp. 2161–2166, Nov. 2000.

[12] Y. Sun, S. E. Thompson, and T. Nishida, "Physics of strain effects in semiconductors and metal–oxide–semiconductor field-effect transistors," *J. Appl. Phys.*, vol. 101, no. 10, p. 104 503, May 2007.
[13] T. Low, M. F. Li, Y. C. Yeo, W. J. Fan, S. T. Ng, and D. L. Kwong, "Valence band structure of ultrathin silicon and germanium channels in metal–oxide–semiconductor field-effect transistors," *J. Appl. Phys.*, vol. 98, no. 2, p. 024 504, Jul. 2005.

Ming-Jer Chen (S'78–M'79–SM'98) received the B.S. degree in electrical engineering (with highest honors) from National Cheng Kung University, Tainan, Taiwan, in 1977 and the M.S. and Ph.D. degrees in electronics engineering from National Chiao Tung University (NCTU), Hsinchu, Taiwan, in 1979 and 1985, respectively.

In 1985, he joined the Department of Electronics Engineering, NCTU, and became a Full Professor in 1993. From 1987 to 1992, he was a Consultant for the Taiwan Semiconductor Manufacturing Company, where he led a team from the NCTU and the Electronics Research and Service Organization/Industrial Technology Research Institute to build up a series of process windows and design rules. From 2000 to 2001, he was a Visiting Professor with the Department of Electrical Engineering and the Center for Integrated Systems, Stanford University, Stanford, CA. He is the holder of eight U.S. patents and six Taiwanese patents in the field of the high-precision analog capacitors, 1-T memory cell, dynamic threshold metal–oxide–semiiconductor, electrostatic discharge protection, and Flash memory. He has graduated 16 Ph.D. students and more than 100 M.S. students. His current research interests are device physics, trap physics, and reliability physics, all in the area of nanoelectronics.

Dr. Chen is a member of the Phi Tau Phi.

Chien-Chih Lee (S'07) was born in Taipei, Taiwan, in 1981. He received the B.S. degree in physics from National Chung Hsing University, Taichung, Taiwan, in 2004. He is currently working toward the Ph.D. degree in electronics engineering with the Department of Electronics Engineering and Institute of Electronics, National Chiao Tung University, Hsinchu, Taiwan.

His research interests include the characterization and modeling of the strained devices, the development of the quantum simulator, and the study of the trap physics in nanoscale devices.

Kuan-Hao Cheng was born in Kaohsiung, Taiwan, in 1984. He received the B.S. degree in electrical engineering from National Chung Cheng University, Chiayi, Taiwan, in 2008 and the M.S. degree in electronics engineering from National Chiao Tung University, Hsinchu, Taiwan, in 2010.

He is currently with the Ministry of National Defense, Taipei, Taiwan, where he is performing the military service. His research interest is the quantum simulation of the strained devices.